Received: 4 July 2024 | Accepted: 14 October 2024

DOI: 10.1097/HC9.0000000000000593

ORIGINAL ARTICLE

OPEN

Vessels encapsulating tumor clusters contribute to the intratumor heterogeneity of HCC on Gd-EOB-DTPA–enhanced MRI

Kosuke Matsuda[1,2] | **Akihisa Ueno**[1,3] | **Junya Tsuzaki**[4] | **Yutaka Kurebayashi**[1] | **Yohei Masugi**[1,3] | **Ken Yamazaki**[1] | **Masashi Tamura**[4] | **Yuta Abe**[5] | **Yasushi Hasegawa**[5] | **Minoru Kitago**[5] | **Masahiro Jinzaki**[4] | **Michiie Sakamoto**[1,6]

[1]Department of Pathology, Keio University School of Medicine, Tokyo, Japan

[2]Department of Pathology, Brigham and Women's Hospital, Harvard Medical School, Boston, Massachusetts, USA

[3]Division of Diagnostic Pathology, Keio University Hospital, Tokyo, Japan

[4]Department of Radiology, Keio University School of Medicine, Tokyo, Japan

[5]Department of Surgery, Keio University School of Medicine, Tokyo, Japan

[6]School of Medicine, International University of Health and Welfare, Chiba, Japan

Correspondence
Akihisa Ueno, Department of Pathology, Keio University School of Medicine, 35 Shinanomachi, Shinjuku-ku, Tokyo 160-0016, Japan. Email: akihisaueno@keio.jp

Michiie Sakamoto, School of Medicine, International University of Health and Welfare, 4-3 Kozunomori, Narita-shi, Chiba 286-8686, Japan. Email: msakamot@z5.keio.jp

Abstract

Background: Vessels encapsulating tumor clusters (VETC) pattern is tumor vasculature of HCC and is a predictor of prognosis and therapeutic efficacy. Recent radiological studies have demonstrated the predictability of VETC from preoperative images, but the mechanisms of image formation are not elucidated. This study aims to determine the relationship between VETC and intratumor heterogeneity in Gd-EOB-DTPA–enhanced magnetic resonance imaging (EOB-MRI) and to provide its pathological evidence.

Methods: Radiologists visually classified preoperative arterial- and hepatobiliary-phase EOB-MRI images of 204 surgically resected HCCs into patterns based on heterogeneity and signal intensity; these classifications were validated using texture analysis. Single and multiplex immunohistochemistry for CD34, h-caldesmon, and OATP1B3 were performed to evaluate VETC, arterial vessel density (AVD), and OATP1B3 expression. Recurrence-free survival was assessed using the generalized Wilcoxon test. The contribution of clinicoradiological factors to the prediction of VETC was evaluated by random forest and least absolute shrinkage and selection operator regression.

Results: VETC was frequently found in tumors with arterial-phase heterogeneous hyper-enhancement patterns and in tumors with hepatobiliary-phase

Abbreviations: AP, arterial phase; AR, androgen receptor; AVD, arterial vessel density; GLDM, gray level dependence matrix; GLRLM, gray level run length matrix; GLSZM, gray level size zone matrix; HBP, hepatobiliary phase; HBP-PH, hepatobiliary phase peritumoral hypointensity; LASSO, least absolute shrinkage and selection operator; OATP1B3, organic anion transporting peptide 1B3; OER, OATP1B3 expression ratio; RER, relative enhancement ratio; RFS, recurrence-free survival; VETC, vessels encapsulating tumor clusters; W/B, WNT/β-catenin pathway-activated.

Akihisa Ueno and Michiie Sakamoto are co-corresponding authors.

Preliminary findings of this study were presented at the AACR annual meeting 2024.

Supplemental Digital Content is available for this article. Direct URL citations are provided in the HTML and PDF versions of this article on the journal's website, www.hepcommjournal.com.

heterogeneous hyperintense/isointense patterns (HBP-Hetero). AVD and OATP1B3 expression positively correlated with signal intensity in the arterial and hepatobiliary phases, respectively. Intratumor spatial analysis revealed that AVD and OATP1B3 expression were lower in VETC regions than in tumor regions without VETC. Patients with HBP-Hetero tumors had shorter recurrence-free survival. Machine learning models highlighted the importance of serum PIVKA-II, tumor size, and enhancement pattern of arterial and hepatobiliary phase for VETC prediction.

Conclusions: VETC is associated with local reductions of both AVD and OATP1B3 expression, likely contributing to heterogeneous enhancement patterns in EOB-MRI. Evaluation of the arterial and hepatobiliary phases of EOB-MRI would enhance the predictability of VETC.

Keywords: arterial vessel density, machine learning, multiple immunofluorescence, organic anion transporting peptide 1B3 (OATP1B3), WNT/β-catenin activation

INTRODUCTION

The tumor microenvironment of HCC is receiving increased attention because recently developed treatments against advanced HCC, including combined immunotherapy (atezolizumab plus bevacizumab) and tyrosine kinase inhibitors, also target tumor angiogenesis and immune cells.[1] Although these therapies require appropriate patient stratification based on the states of tumor angiogenesis and immune reaction, it remains difficult to determine the tumor microenvironment without pathological examinations. Progress in texture analysis of radiological images has shown that intratumor heterogeneity correlates with clinical prognosis on CT[2–4] and MRI; moreover, recent studies have suggested that intratumor heterogeneity in pretreatment radiological images may predict specific histological structures.[5–7] In particular, texture analyses in preoperative gadolinium-ethoxybenzyl-diethylenetriamine pentaacetic acid-enhanced MRI (EOB-MRI) have recently suggested a correlation between kurtosis and nonuniformity, which are indices of heterogeneity, and vessels encapsulating tumor cluster (VETC) structure.[8–11]

VETC structure, a distinctive tumor vasculature in which vascular endothelium covers tumor foci, has attracted attention as a histological index that reflects the tumor microenvironment. VETC is reportedly induced by angiopoietin 2 and correlates with angiogenic status, reduced lymphocytic infiltration, and a worse prognosis after surgical resection.[12–14] Furthermore, it has been suggested that VETC may be a predictor of the clinical prognosis and therapeutic response to tyrosine kinase inhibitors and immunotherapies.[13,15,16] Because of the clinical importance of VETC, several studies have attempted to detect HCC that contains VETC structure ($VETC^+$ HCC) by using preoperative radiological imaging.[8–11,17] However, the histopathological background and mechanisms that form these radiological images remain unclear.

Against this background, we hypothesized that VETC may contribute to intratumor heterogeneity on radiological images with some histological changes. To test this hypothesis, we compared the status and intratumor distribution of VETC structures with the intratumor heterogeneity of EOB-MRI findings, in which arterial-phase images reflect the dynamics of arterial blood flow and the density of unpaired arteries in tumor tissue,[18] whereas hepatobiliary-phase images reflect the tumor biology, for example, the expression of organic anion transporting polypeptide 1B3 (OATP1B3) and WNT/β-catenin pathway activation.[19]

METHODS

Patients and samples

This study was conducted in accordance with the principles of the 2013 Declaration of Helsinki and the 2018 Declaration of Istanbul and was approved by the Ethics Committee of Keio University School of Medicine (approval number: 20040034). Written informed consent was obtained from each patient who participated in this study. Between 2008 and 2020, 484 HCCs were surgically resected from 325 patients at Keio University Hospital (Tokyo, Japan). Tumors that met the following criteria were excluded from the

present cohort: metastatic recurrence, tumors with severe necrotic change, tumors with components of glandular differentiation, and tumors in the livers of recipients of transplant. Of the remaining cases, 204 HCCs from 183 patients with preoperative EOB-MRI data were included in the current study. The survival analysis included 134 of these 183 patients; patients with multiple or recurrent HCCs and those with <60 days of follow-up were excluded from the survival analysis (Supplemental Figure S1, http://links.lww.com/HC9/B151). The clinical outcomes of the patients were extracted retrospectively from electronic medical records. Recurrence-free survival (RFS) was defined as the interval between surgical resection and an initial radiological diagnosis of recurrence. The median follow-up period of the 134 cases included in the survival analysis was 678 days (range, 70–4371 d).

MRI analysis

The MRI systems used in this study were 1.5-T (Signa ES, Signa HD, Sign HDxt, Signa Excite, or Optima MR450W, GE Healthcare) or 3-T systems (Discovery MR750 or Signa Pioneer, GE Healthcare). The MRI scanning protocols were similar to those used in our previous study.[19,20] Visual evaluations of EOB-MRI were performed by mutual agreement of 2 abdominal radiologists (Junya Tsuzaki and Masashi Tamura). Based on the procedures described in previous reports,[5,21] we classified arterial-phase images into 4 patterns and hepatobiliary-phase images into 5 patterns and evaluated the presence of 4 ancillary findings from LI-RADS version 2018,[21,22] namely intratumor artery in arterial phase, arterial phase peritumoral enhancement, non-smooth tumor margin, and hepatobiliary phase peritumoral hypointensity (HBP-PH).

Arterial-phase images were visually classified into the following 4 patterns: homogenously hyper-enhancement (AP-Homo), heterogeneously hyper-enhancement (AP-Hetero), hypo-enhancement (AP-Hypo), and rim-like (AP-Rim) (Figure 1A). Hepatobiliary-phase images were visually classified into the following 5 patterns: homogenously hyperintense (HBP-Homo/hyper), heterogeneously hyperintense (HBP-Hetero/hyper), homogenously isointense (HBP-Homo/iso), heterogeneously isointense (HBP-Hetero/iso), and hypointense (HBP-Hypo) (Figure 2A). Hyperintensity was defined as an intensity equal to or greater than that of nontumorous liver, isointensity was defined as an intensity below that of nontumorous liver but enhanced compared to that in precontrast images, and hypointensity was defined as neither hyperintense nor isointense.

The visual assessment of intensity was validated using the relative enhancement ratio (RER), that is, the intensity of tumor to nontumorous liver in each phase relative to that in precontrast images.[23] The assessment of heterogeneity was validated using texture analysis. The detailed method for texture analysis is described in the Supplemental Materials and Methods section, http://links.lww.com/HC9/B151.

Histopathological analysis

Hematoxylin and eosin staining was carried out on formalin-fixed, paraffin-embedded sections of all resected specimens. Histological analyses of HCCs were performed by at least 2 liver pathologists (finalized by Michiie Sakamoto), according to the fifth edition of the World Health Organization classification of 2019.[24] We documented histologic features such as tumor grade, microvascular invasion, and intrahepatic metastasis. The proportion of macrotrabecular pattern was measured in 10% increments, and macrotrabecular massive-HCCs were defined as the proportion exceeding 50%.[25] The stage of liver fibrosis in the nontumorous liver was defined according to the METAVIR classification.[26]

Immunohistochemical staining

For immunohistochemical analysis, representative formalin-fixed, paraffin-embedded tissue blocks were selected for each nodule, and 4-μm-thick sections were prepared. Immunohistochemical staining was performed using a Bond-Max Automated Stainer (Leica Microsystems). Staining was performed for the following markers: CD34, OATP1B3, h-caldesmon, β-catenin, glutamine synthetase, cytokeratin 19, and Ki-67. The antibodies used in this study are listed in Supplemental Table S1, http://links.lww.com/HC9/B151. The detailed method for multiplex fluorescence immunohistochemistry is given in the Supplemental Materials and Methods section, http://links.lww.com/HC9/B151.

Immunohistochemical evaluation

VETC was evaluated in a manner similar to that used in our previous study,[12] with areas surrounded by endothelial cells defined as VETC-positive if they occupied more than 1% of the tumor area.

The arterial vessel density (AVD) was determined manually by counting vessels with h-caldesmon–positive walls in 5 representative high-power (×200) fields (×20 objective lens and ×10 ocular lens; 0.7386 mm^2 per field).[27] However, vessels positive for h-caldesmon were not counted if they were in the portal region or in a thick capsule or septum. Furthermore, h-caldesmon–positive structures that were not vessels were excluded.

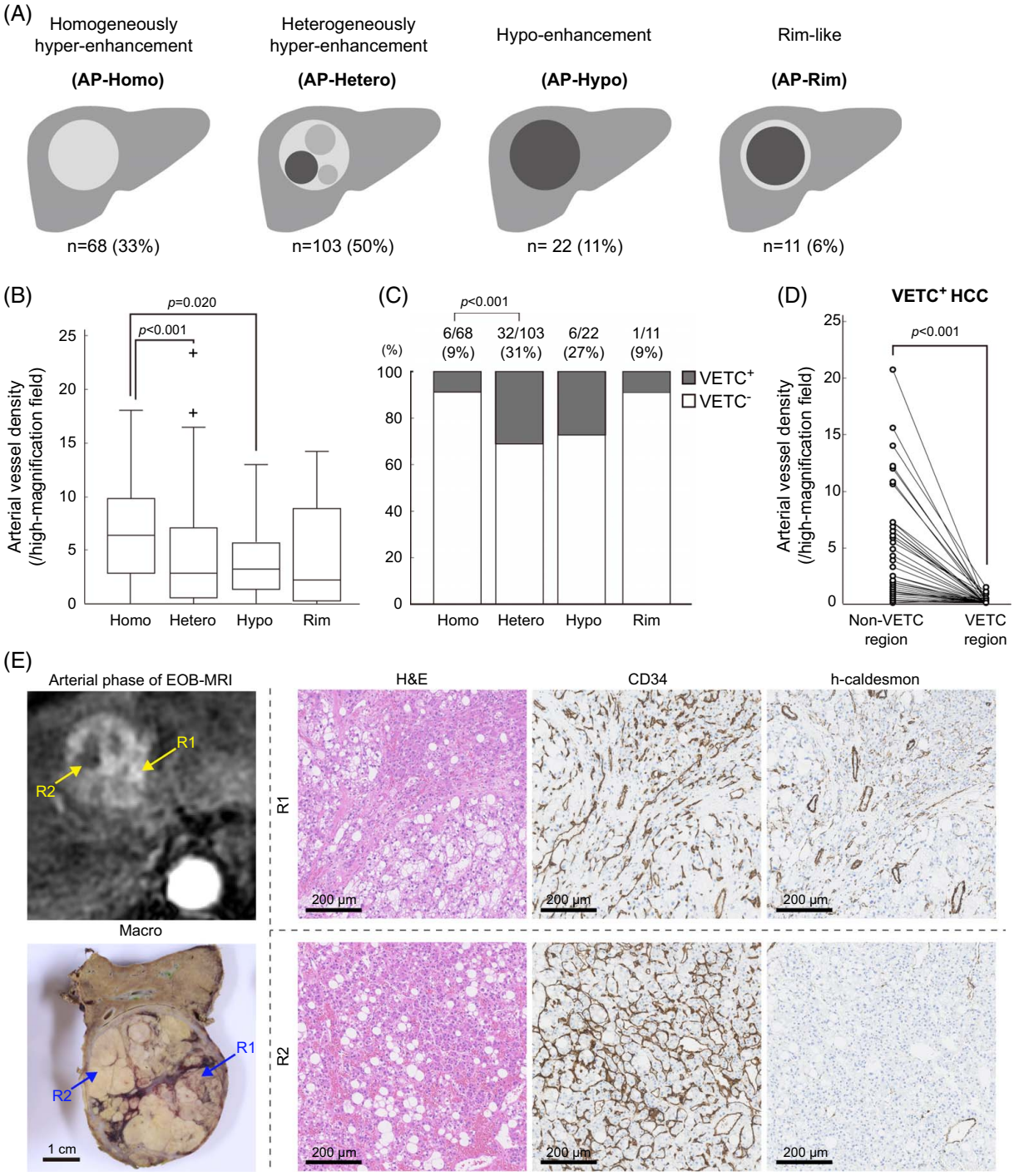

FIGURE 1 Heterogeneous tumors in the arterial phase of EOB-MRI have a low AVD and high VETC positivity. (A) Schema of each enhancement pattern. (B) AP-Hetero pattern and AP-Hypo pattern tumors had lower AVD than AP-Homo tumors (Mann-Whitney *U* test). (C) AP-Hetero tumors had higher VETC positivity than AP-Homo tumors (χ^2 test). (D) Among VETC$^+$ HCCs, regions with VETC had lower AVD than regions without VETC (Wilcoxon signed-rank test). (E) A case of VETC$^+$ HCC with AP-Hetero pattern. Strongly enhanced region R1 had no VETC structures but abundant h-caldesmon–positive arteries, whereas weakly enhanced region R2 showed VETC structures but few arteries. Abbreviations: AVD, arterial vessel density; VETC, vessels encapsulating tumor clusters.

For OATP1B3, the proportion score was defined using the area percentage of OATP1B3 expression in the tumor (0: 0%, 1: 1%–33%, 2: 34%–66%, and 3: 67%–100%). The intensity score was defined as the intensity of OATP1B3 staining in the tumor compared to that of zone 3 in nontumorous liver (0: negative, 1: weak, 2: equivocal, and 3: strong) (Supplemental Figure S2A, http://links.lww.com/HC9/B151). The latter is

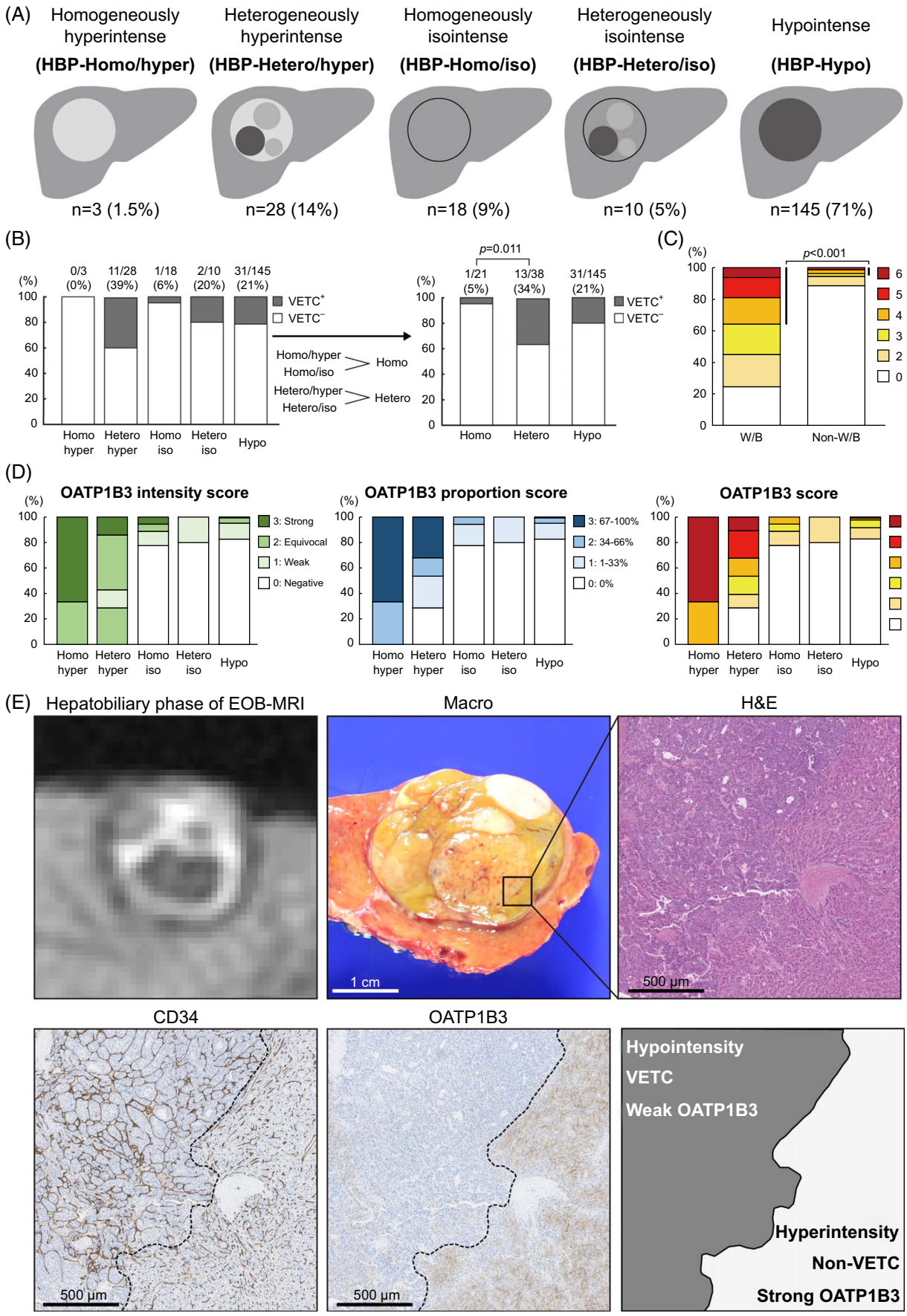
(A)
Homogeneously hyperintense (HBP-Homo/hyper)
Heterogeneously hyperintense (HBP-Hetero/hyper)
Homogeneously isointense (HBP-Homo/iso)
Heterogeneously isointense (HBP-Hetero/iso)
Hypointense (HBP-Hypo)
n=3 (1.5%)
n=28 (14%)
n=18 (9%)
n=10 (5%)
n=145 (71%)
(B)
0/3 (0%)
11/28 (39%)
1/18 (6%)
2/10 (20%)
31/145 (21%)
VETC+
VETC−
Homo/hyper
Homo/iso
Homo
Hetero/hyper
Hetero/iso
Hetero
Homo hyper
Hetero hyper
Homo iso
Hetero iso
Hypo
p=0.011
1/21 (5%)
13/38 (34%)
31/145 (21%)
Homo
Hetero
Hypo
(C)
p<0.001
W/B
Non-W/B
(D)
OATP1B3 intensity score
3: Strong
2: Equivocal
1: Weak
0: Negative
OATP1B3 proportion score
3: 67-100%
2: 34-66%
1: 1-33%
0: 0%
OATP1B3 score
(E)
Hepatobiliary phase of EOB-MRI
Macro
H&E
1 cm
500 μm
CD34
OATP1B3
Hypointensity
VETC
Weak OATP1B3
Hyperintensity
Non-VETC
Strong OATP1B3

FIGURE 2 Heterogeneous tumors in the hepatobiliary phase of EOB-MRI exhibit heterogeneous OATP1B3 expression and high VETC positivity. (A) Schema of each enhancement pattern. (B) HBP-Hetero pattern tumors had higher VETC positivity than HBP-Homo tumors (χ^2 test). (C) WNT β-catenin pathway–activated (W/B) HCCs showed higher OATP1B3 scores than non-W/B HCCs (χ^2 test). (D) OATP1B3 intensity score, proportion score, and their sum (OATP1B3 score) for each enhancement pattern. (E) A case of VETC$^+$ HCC with HBP-Hetero/hyper pattern. A strongly enhanced region in the hepatobiliary phase (lower right) had no VETC structures but strong OATP1B3 expression, whereas a weakly enhanced region (upper left) showed VETC structures but weak OATP1B3 expression. Abbreviations: OATP1B3, organic anion transporting peptide 1B3; VETC, vessels encapsulating tumor clusters.

similar to the OATP1B3 expression score used in our previous report.[19] The sum of the proportion score and the intensity score was defined as the OATP1B3 score.

The evaluation of β-catenin, glutamine synthetase, cytokeratin 19, and Ki-67 was carried out in a similar way to that described in our previous report (Supplemental Figures S2B, C, http://links.lww.com/HC9/B151).[12]

Quantitative spatial histological analysis

Quantitative histological analysis was conducted using MATLAB version R2023a software (RRID:SCR_001622, Mathworks). Immunohistochemistry images of h-caldesmon were acquired at a magnification of 1.25, and the sizes were 1980 × 1080 pixels. The images were binarized based on the color information, de-noised by morphology filters, and the h-caldesmon–positive areas were measured for each 1 × 1 mm^2 grid (Supplemental Figure S6A, http://links.lww.com/HC9/B151). To assess the heterogeneity of these positive areas in the tumor region, Moran's I, coefficient of variation, and entropy were calculated.[28,29] The coefficient of variation is defined as the ratio of the SD to the mean.[30] For multiplex fluorescence immunohistochemistry images, we annotated tumor and VETC regions on CD34-stained images (Figure 3A). A region was defined as a VETC region if it was located inside the VETC annotation, and the rest of the tumor region was designated the non-VETC region. Further, the region lying ~500 μm outside the VETC region was defined as the peri-VETC region, and the tumor region other than the VETC region and peri-VETC region was defined as the far non-VETC region. We then converted the OATP1B3-stained images to grayscale and defined pixels with intensities above a certain threshold level as positive. This threshold level was determined so that pixels around zone 3 would be positive in the nontumorous liver. The OATP1B3 expression ratio (OER) is defined by the following formula:

$$OATP1B3\ expression\ proportion\ (OEP)_{Region\ X} = \frac{OATP1B3^{+}\ \ pixels\ in\ Region\ X}{Total\ pixels\ in\ Region\ X}$$

$$OATP1B3\ expression\ ratio\ (OER) = \frac{OEP_{VETC}}{OEP_{Non-VETC}}$$

The h-caldesmon–stained images were binarized, expanded, and structured to allow the counting of arterial vessels. AVD was then determined automatically as the number of arterial structures divided by the total pixel count of the area of interest.[31,32] Although the manual and automatic determinations of AVD have different units, that is, arteries per high-magnification field and arteries per pixel, respectively, they are both valid determinations of AVD.

Machine learning model construction and validation

The machine learning model construction and validation were performed using MATLAB software. Feature selection and model development followed the random forest and least absolute shrinkage and selection operator (LASSO) regression algorithms, respectively.[33,34] Details are described in the Supplemental Materials and Methods section, http://links.lww.com/HC9/B151.

Statistical analysis

Unpaired variables were compared using the Student *t* test or the Mann-Whitney *U* test. Paired variables were compared using the Wilcoxon signed-rank test. Categorical variables were compared using the χ^2 test. Kaplan-Meier survival curves and the generalized Wilcoxon test were used to analyze RFS. Intergroup statistical comparison was performed using the above tests with Bonferroni correction. All statistical analyses were performed using SPSS software version 29 (RRID:SCR_002865, IBM Statistics).

RESULTS

Classification by EOB-MRI arterial-phase enhancement patterns and the clinicopathological features of each pattern

Arterial-phase images were visually classified into the following 4 patterns: homogenously hyper-enhancement (AP-Homo), heterogeneously hyper-enhancement

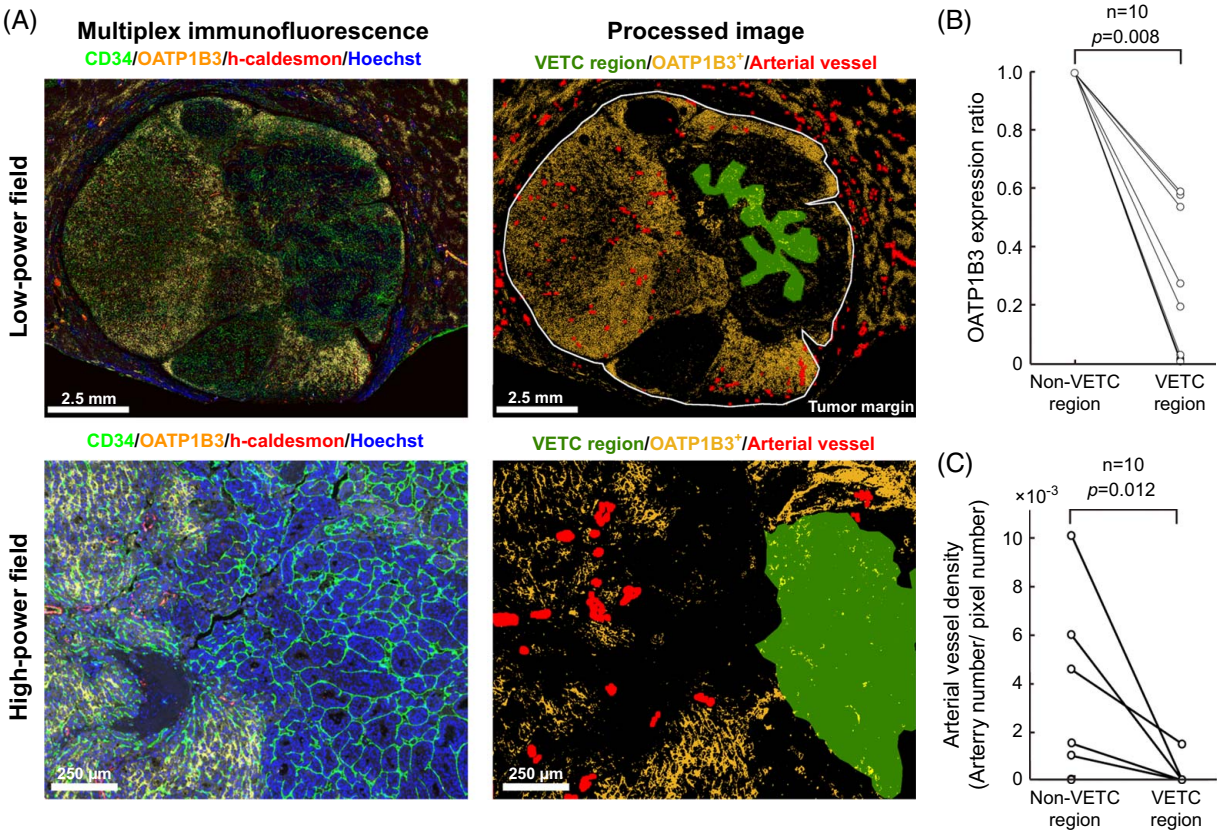

FIGURE 3 Spatial analysis of VETC, OATP1B3, and arterial vessels using multiplex immunofluorescent immunohistochemistry. (A) Based on multiplex immunofluorescence images of CD34, OATP1B3, h-caldesmon, and Hoechst, computational image analysis was used to annotate VETC regions, determine OATP1B3 expression regions, and visualize h-caldesmon$^+$ arteries. (B) VETC regions had lower OATP1B3 expression ratios than non-VETC regions (Wilcoxon signed-rank test). (C) VETC regions had a lower AVD count than non-VETC regions (Wilcoxon signed-rank test). Abbreviations: AVD, arterial vessel density; OATP1B3, organic anion transporting peptide 1B3; VETC, vessels encapsulating tumor clusters.

(AP-Hetero), hypo-enhancement (AP-Hypo), and rim-like (AP-Rim) (Figure 1A). In the current cohort of tumors (n = 204), the AP-Homo pattern was observed in 68 tumors, the AP-Hetero pattern in 103 tumors, the AP-Hypo pattern in 22 tumors, and the AP-Rim pattern in 11 tumors (Figure 1A). The clinicopathological characteristics of each enhancement pattern are shown in Table 1. Compared with AP-Homo tumors, AP-Hetero tumors were correlated with higher levels of PIVKA-II, larger tumor size, poor differentiation, microvascular invasion, intrahepatic metastasis, and VETC. AP-Hypo tumors showed larger tumor size than AP-Homo tumors. AP-Homo tumors did not include macrotrabecular massive-HCC.

Visual assessments were validated using the RER and texture analysis. The RER values of AP-Homo and AP-Hetero tumors were significantly higher than those of AP-Hypo tumors, and the values of indicators of heterogeneity, including GLDM-GrayLevelNonUniformity, GLRLM-GrayLevelNonUniformity, and GLSZM-GrayLevelNonUniformity, were all significantly higher in AP-Hetero tumors than in AP-Homo tumors (Supplemental Figure S3, http://links.lww.com/HC9/B151).

Lower AVD in tumor regions with VETC explains intratumor heterogeneity in the EOB-MRI arterial phase

Because the density of unpaired arteries that lead blood flow to the sinusoidal vessels is expected to correlate with enhancement of the arterial phase, we further investigated the relationship between these arteries and VETC. AVD was significantly lower in AP-Hetero and AP-Hypo tumors than in AP-Homo tumors (Figure 1B). In the current cohort, 45 of 204 HCCs (22%) were classified as VETC$^+$ HCC. The respective VETC positivity rates were 8.8% for AP-Homo, 31% for AP-Hetero, 27% for AP-Hypo, and 9.1% for AP-Rim pattern tumors (Figure 1C). These results prompted us to investigate the relationship between arterial density and VETC within tumors. Among VETC$^+$ HCCs, when measuring AVD in tumor regions with VETC (VETC region) and without VETC (non-VETC region), AVD was clearly lower in the VETC region (Figure 1D). A representative example of an AP-Hetero tumor showed that VETC structure and local reduction in AVD were observed, consistent with the region with local reduction of enhancement in the arterial phase (Figure 1E). In addition,

TABLE 1 Clinicopathological features of each enhancement pattern on the arterial phase of EOB-MRI

	n (%) or median				*p*		
	AP-Homo n = 68	**AP-Hetero n = 103**	**AP-Hypo n = 22**	**AP-Rim n = 11**	**Homo vs. Hetero**	**Homo vs. Hypo**	**Hetero vs. Hypo**
Age (y)	72 (67–77)	72 (65–77)	72 (67–76)	68 (61–72)	0.405	0.981	0.645
Sex					0.204	0.411	0.116
Male	57 (84)	78 (76)	20 (91)	8 (73)			
Female	11 (16)	25 (24)	2 (9)	3 (27)			
Etiology					0.063	0.693	0.571
Hepatitis B	16 (23)	25 (24)	4 (18)	1 (9)			
Hepatitis C	26 (38)	21 (20)	7 (32)	2 (18)			
Hepatitis B and C	1 (2)	3 (3)	0	0			
Others	25 (37)	54 (53)	11 (50)	8 (73)			
AFP, ng/mL					0.055	0.022	0.413
>300	4 (6)	16 (16)	5 (23)	3 (27)			
≤ 300	64 (94)	87 (84)	17 (77)	8 (73)			
PIVKA-II, ng/mL					0.0014**	0.016	0.676
>400	9 (13)	42 (41)	8 (37)	5 (46)			
≤ 400	59 (67)	61 (59)	14 (63)	6 (54)			
Tumor size, mm					<0.0000167***	0.013	0.226
>50	2 (3)	32 (31)	4 (18)	2 (18)			
≤ 50	66 (97)	71 (69)	18 (82)	9 (82)			
Differentiation					0.00082**	0.0014**	0.317
Well	9 (13)	12 (12)	5 (23)	0			
Moderately	58 (85)	71 (69)	12 (54)	9 (82)			
Poorly	1 (2)	20 (19)	5 (23)	2 (18)			
Microvascular invasion					0.00099**	0.066	0.762
Positive	28 (41)	69 (67)	14 (63)	8 (73)			
Negative	40 (59)	34 (33)	8 (37)	3 (27)			
Intrahepatic metastasis					0.0029*	0.083	0.497
Positive	1 (2)	15 (15)	2 (9)	3 (27)			
Negative	67 (98)	88 (85)	20 (91)	8 (73)			
VETC					0.00061**	0.027	0.725
Positive	6 (9)	32 (31)	6 (27)	1 (9)			
Negative	62 (91)	71 (69)	16 (63)	10 (91)			
Macrotrabecular massive					0.072	0.550	1.000
Yes	0	7 (7)	1 (5)	1 (9)			
No	68 (100)	96 (93)	21 (95)	10 (81)			
β-Catenin					0.109	0.870	0.248
Nuclear positive	7 (10)	20 (19)	2 (9)	2 (18)			
Not nuclear positive	61 (90)	83 (81)	20 (91)	9 (82)			
GS					0.204	0.485	0.878
Diffuse positive	11 (16)	25 (24)	5 (23)	3 (27)			
Not diffuse positive	57 (84)	78 (76)	17 (77)	8 (73)			

TABLE 1. (*continued*)

	n (%) or median				*p*		
	AP-Homo n = 68	AP-Hetero n = 103	AP-Hypo n = 22	AP-Rim n = 11	Homo vs. Hetero	Homo vs. Hypo	Hetero vs. Hypo
WNT/β-catenin activation					0.264	0.831	0.604
Positive	14 (21)	29 (28)	5 (23)	3 (27)			
Negative	54 (79)	74 (72)	17 (77)	8 (73)			
CK19					0.071	0.016	0.378
Positive	1 (2)	8 (8)	3 (14)	3 (27)			
Negative	67 (98)	95 (92)	19 (86)	8 (73)			
Ki-67					0.024	0.299	0.604
Labeling index >30%	9 (13)	29 (28)	5 (23)	4 (36)			
Labeling index ≤30%	59 (87)	74 (72)	17 (77)	7 (64)			
METAVIR-F					0.070	0.241	0.981
0–2	33 (49)	64 (63)	8 (36)	2 (20)			
3–4	34 (51)	37 (37)	14 (64)	8 (80)			
Not assessable	1	2	0	1			

*$p < 0.0083$.
**$p < 0.00167$.
***$p < 0.000167$ (χ^2 test and Mann-Whitney U test with Bonferroni correction).
Abbreviations: AP, arterial phase; CK19, cytokeratin 19; GS, glutamine synthetase; Hetero, heterogeneously hypervascular; Homo, homogeneously hypervascular; Hypo, hypovascular; METAVIR-F, fibrosis score; Rim, rim-like pattern; VETC, vessels encapsulating tumor clusters.

we validated the correlation between arterial vessel heterogeneity in tissue and heterogeneity in arterial-phase images. Moran's I and coefficient of variation, calculated as measures of heterogeneity in the distribution of h-caldesmon–positive arteries, were significantly higher in AP-Hetero tumors than in AP-Hypo tumors. Entropy, calculated similarly, showed no significant difference in the contrast patterns (Supplemental Figure S4, http://links.lww.com/HC9/B151).

Classification by hepatobiliary-phase EOB-MRI enhancement patterns and the clinicopathological features of each pattern

Hepatobiliary-phase images were visually classified into the following 5 patterns: homogenously hyperintense (HBP-Homo/hyper), heterogeneously hyperintense (HBP-Hetero/hyper), homogenously isointense (HBP-Homo/iso), heterogeneously isointense (HBP-Hetero/iso), and hypointense (HBP-Hypo). The HBP-Homo/hyper pattern was observed in 3 tumors, HBP-Hetero/hyper pattern in 28 tumors, HBP-Homo/iso pattern in 18 tumors, HBP-Hetero/iso pattern in 10 tumors, and HBP-Hypo pattern in 145 tumors (Figure 2A). Because the frequencies of HBP-Homo/hyper and HBP-Hetero/iso patterns were low (≤10% for both), and both hyper (HBP-Homo/hyper and HBP-Hetero/hyper) patterns and iso (HBP-Homo/iso and HBP-Hetero/iso) patterns had significantly higher RER values than HBP-Hypo tumors (Supplemental Figure S5A, http://links.lww.com/HC9/B151), statistical analysis was performed as HBP-Homo for HBP-Homo/hyper and HBP-Homo/iso combined and as HBP-Hetero for HBP-Hetero/hyper and HBP-Hetero/iso combined.

The clinicopathological characteristics of each enhancement pattern are shown in Table 2. VETC pattern was observed more frequently in HBP-Hetero tumors than in HBP-Homo tumors. Large tumor size and WNT/β-catenin activation (defined immunohistochemically as nuclear positive for β-catenin or diffuse positive for glutamine synthetase) were observed more frequently in HBP-Hetero tumors than in HBP-Hypo tumors. The respective VETC positivity rates were 4.7% for HBP-Homo tumors, 34% for HBP-Hetero tumors, and 21% for HBP-Hypo tumors. VETC positivity was higher in HBP-Hetero tumors than in HBP-Homo tumors (Figure 2B). Texture analysis confirmed that the indicators of heterogeneity were all significantly higher in HBP-Hetero tumors than in HBP-Homo tumors (Supplemental Figure S5B, http://links.lww.com/HC9/B151), thereby validating the findings of visually assessed heterogeneity.

TABLE 2 Clinicopathological features of each enhancement pattern on the hepatobiliary phase of EOB-MRI

	n (%) or median			*p*		
	HBP-Homo n = 21	**HBP-Hetero n = 38**	**HBP-Hypo n = 145**	**Homo vs. Hetero**	**Homo vs. Hypo**	**Hetero vs. Hypo**
Age (y)	74 (68–76)	72 (68–74)	71 (65–77)	0.451	0.299	0.565
Sex				0.449	0.743	0.499
Male	16 (76)	32 (84)	115 (79)			
Female	5 (24)	6 (16)	30 (21)			
Etiology				0.572	0.530	0.061
Hepatitis B	6 (29)	7 (18)	33 (23)			
Hepatitis C	4 (19)	6 (16)	46 (32)			
Hepatitis B and C	0	0	4 (3)			
Others	11 (52)	25 (66)	62 (43)			
AFP, ng/mL				0.096	0.272	0.219
>300	1 (5)	8 (21)	19 (13)			
≤ 300	20 (95)	30 (79)	126 (87)			
PIVKA-II, ng/mL				0.155	0.237	0.550
>400	4 (19)	14 (37)	8 (6)			
≤ 400	17 (81)	24 (63)	137 (94)			
Tumor size, mm				0.099	0.793	0.016*
>50	3 (14)	13 (34)	24 (17)			
≤ 50	18 (86)	25 (66)	121 (83)			
Differentiation				0.176	0.044	0.055
Well	6 (29)	4 (11)	16 (11)			
Moderately	14 (66)	33 (87)	103 (71)			
Poorly	1 (5)	1 (3)	26 (18)			
Microvascular invasion				0.024	0.077	0.271
Positive	8 (38)	26 (68)	85 (59)			
Negative	13 (62)	12 (32)	60 (41)			
Intrahepatic metastasis				0.878	0.369	0.166
Positive	3 (14)	6 (16)	12 (8)			
Negative	18 (86)	32 (84)	133 (92)			
VETC				0.011*	0.071	0.099
Positive	1 (5)	13 (34)	31 (21)			
Negative	20 (95)	25 (66)	114 (79)			
Macrotrabecular massive				1.000	1.000	1.000
Yes	1 (5)	2 (5)	6 (4)			
No	20 (95)	36 (95)	139 (96)			
β-Catenin				0.205	0.736	0.009*
Nuclear positive	3 (14)	11 (29)	17 (12)			
Not nuclear positive	18 (86)	27 (71)	128 (88)			
GS				0.076	0.272	0.000072***
Diffuse positive	5 (24)	18 (47)	21 (14)			
Not diffuse positive	16 (76)	20 (53)	124 (86)			
WNT/β-catenin activation				0.296	0.098	0.00044**
Positive	7 (33)	18 (47)	26 (18)			
Negative	14 (67)	20 (53)	119 (82)			

TABLE 2. (*continued*)

	n (%) or median			*p*		
	HBP-Homo n = 21	HBP-Hetero n = 38	HBP-Hypo n = 145	Homo vs. Hetero	Homo vs. Hypo	Hetero vs. Hypo
CK19				0.933	0.575	0.534
Positive	1 (5)	2 (5)	12 (8)			
Negative	20 (95)	36 (95)	133 (92)			
Ki-67				0.096	0.029	0.501
Labeling index > 30%	1 (5)	6 (16)	38 (26)			
Labeling index ≤ 30%	20 (95)	32 (84)	107 (74)			
METAVIR-F				0.155	0.110	0.921
0–2	9	14 (38)	87 (61)			
3–4	12	23 (62)	55 (39)			
Not assessable	0	1	3			

*$p < 0.017$.
**$p < 0.0033$.
***$p < 0.00033$ (χ^2 test and Mann-Whitney *U* test with Bonferroni correction).
Abbreviations: CK19, cytokeratin 19; GS, glutamine synthetase; HBP, hepatobiliary phase; Hetero, heterogeneously hyperintense/isointense; Homo, homogeneously hyperintense/isointense; Hypo, hypointense; METAVIR-F, fibrosis score; VETC, vessels encapsulating tumor clusters.

Relationship between OATP1B3 expression and hepatobiliary-phase EOB-MRI enhancement patterns

Because VETC was correlated with heterogeneous patterns in the hepatobiliary phase, we examined the association between OATP1B3, which induces strong enhancement in the hepatobiliary phase of EOB-MRI and VETC. When OATP1B3 expression was evaluated immunohistochemically, WNT β-catenin pathway–activated (W/B) HCCs showed higher OATP1B3 scores than non-W/B HCCs (Figure 2C). The OATP1B3 intensity score, the OATP1B3 proportion score, and the OATP1B3 score were all lower in HBP-Hetero/hyper tumors than in HBP-Homo/hyper tumors (Figure 2D). Furthermore, a comparison of radiological and histopathological images of HBP-Hetero/hyper tumors showed that there were localized decreases of OATP1B3 expression in VETC regions, consistent with areas of locally reduced enhancement (Figure 2E).

Spatial analysis showed decreased OATP1B3 expression and AVD in VETC regions

To complete the analysis, we investigated the spatial relationships among AVD, OATP1B3 expression, and VETC distribution in whole-tissue sections. Among our cohort, there were 10 cases with VETC-positive and high OATP1B3 expression (OATP1B3 score ≥ 4), all of which underwent multiplex immunohistochemistry-based computational analysis. VETC and tumor regions were annotated on CD34-stained images, OATP1B3-stained images were binarized, and the OER was calculated. OER was significantly smaller than 1 in VETC regions (Figure 3B). Furthermore, when the non-VETC region was divided into a peri-VETC region and a far non-VETC region, the peri-VETC region showed lower OER than the far non-VETC region (Supplemental Figure S6, http://links.lww.com/HC9/B151). In addition, h-caldesmon–stained images were binarized and structured to allow the digital measurement of AVD, and AVD was found to be significantly lower in VETC regions than in non-VETC regions (Figure 3C).

Development and validation of random forest model for preoperatively prediction of VETC

Machine learning models were developed to identify clinicoradiological factors important for the preoperative prediction of VETC. In the random forest model, the top 5 features in terms of feature importance were selected: PIVKA-II, tumor size, AP pattern, non-smooth tumor margin, and RER (HBP). In the LASSO regression model, PIVKA-II, tumor size, AP pattern, HBP pattern, and intratumor artery in arterial phase were selected (Supplemental Figures S7B–D, http://links.lww.com/HC9/B151). The random forest model had AUC = 0.88 for the training cohort and AUC = 0.75 for the validation cohort, while the LASSO regression model had AUC = 0.82 for the training cohort and AUC = 0.79 for the validation cohort (Supplemental Figure S7E, http://links.lww.com/HC9/B151).

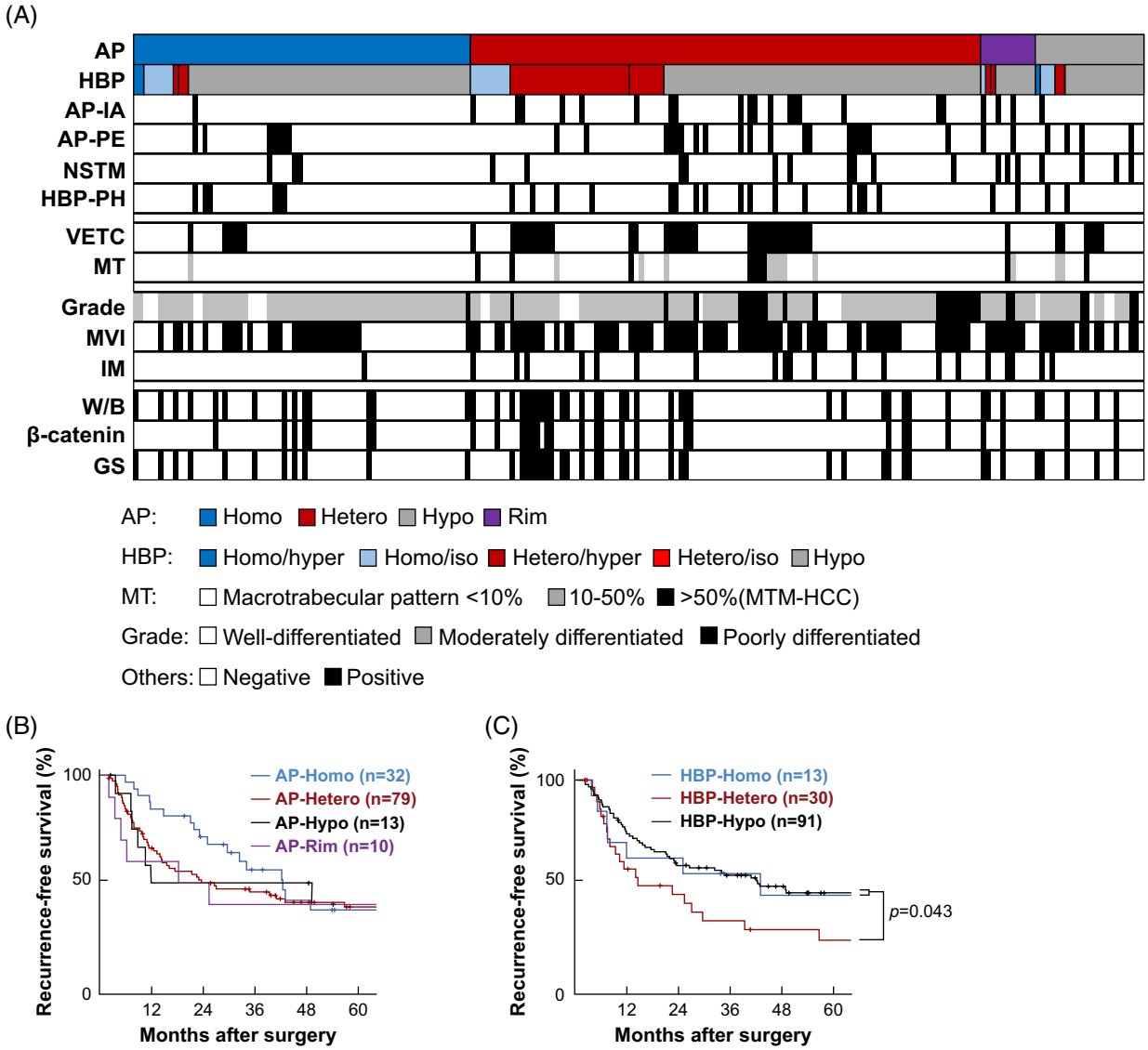

FIGURE 4 Relationship between enhancement patterns on the arterial and hepatobiliary phase of EOB-MRI and clinicopathological factors. (A) Enhancement patterns and pathological factors in 204 cases of HCC. (B, C) Kaplan-Meier curves of recurrence-free survival for patients with each enhancement pattern in the arterial phase (B) and in the hepatobiliary phase (C) (generalized Wilcoxon's test).

Relationship of the contrast patterns to clinical, radiological, and pathological factors

The relationships among EOB-MRI enhancement patterns, VETC, and other histopathological findings are illustrated in Figure 4A. Overall, 84% (31/37) of HBP-Hetero pattern tumors also had the AP-Hetero pattern. The group with both HBP-Homo and AP-Homo patterns did not include any VETC$^+$ HCCs. VETC$^+$ HCCs were more common in AP-Hetero and HBP-Hetero tumors, as described above, and were seen in 7 of 11 tumors with 10%–50% macrotrabecular pattern and 8 of 9 macrotrabecular massive-HCCs (Supplemental Figure S8, http://links.lww.com/HC9/B151). Texture analysis by PyRadiomics revealed that features such as NonUniformity and Entropy, indicators of heterogeneity, were higher in VETC$^+$ HCCs (Supplemental Tables S2 and S3, http://links.lww.com/HC9/B151).

VETC is associated with poor prognosis and a distinctive tumor microenvironment,[12–14] and so the relationship between EOB-MRI enhancement patterns and clinical prognosis was examined. Although there were no significant differences in RFS for patients with different enhancement patterns in the arterial phase, patients with AP-Homo pattern tumors tended to have longer RFS than patients with other patterns ($p = 0.068$; Figure 4B). Furthermore, patients with AP-Homo pattern tumors had a lower recurrence rate within 2 years after surgery than the others ($p = 0.014$). In a classification based on the hepatobiliary phase, patients with the HBP-Hetero pattern had a significantly shorter RFS than those with the HBP-Homo or HBP-Hypo patterns (Figure 4C).

DISCUSSION

In the current study, we have revealed that VETC$^+$ HCC correlates with heterogeneous contrast patterns in the arterial and hepatobiliary phases of EOB-MRI, and histologically, VETC is associated with locally reduced AVD and OATP1B3 expression. HCC is a hypervascular tumor, being rich in unpaired arteries and, therefore, strongly enhanced in the arterial phase; however, the enhancement pattern is sometimes heterogeneous.[18,35] In the current study, few arteries were seen in the VETC region, suggesting that a local reduction in arteries contributes to some of the radiological heterogeneity. Angiogenic factors such as angiopoietin 2 are required for the formation of VETC,[12,14] and it is possible that hypoxia in regions with few arteries may further enhance the expression of angiogenic factors and contribute to VETC formation.

About 15%–30% of HCCs reportedly show high signal intensity in the hepatobiliary phase of EOB-MRI, and some of these show heterogeneous enhancement patterns.[19,36,37] The signal intensity in the hepatobiliary phase is dependent on the expression of OATP1B3, a transporter of Gd-EOB-DTPA[19]; in the current study, reduced OATP1B3 expression was observed not only in the VETC region itself but also in the peri-VETC region. Therefore, reduced OATP1B3 expression may result in changes significant enough to be recognized on radiological images, suggesting that reduced enhancement in VETC and peri-VETC regions contributes to radiological heterogeneity. Zhou et al[38] reported that androgen receptor (AR) expression inhibits the formation of VETC by suppressing angiopoietin 2, and the relationship between reduced OATP1B3 expression and VETC formation may be explained by AR. AR is a member of the nuclear hormone receptor superfamily and undergoes conformational change and translocates to the nucleus when it is bound to androgens in the cytoplasm.[39] Since OATP1B3 is a transporter that facilitates the intracellular uptake of androgens,[40] it may suppress VETC formation through activation of AR.

It has long been noted that radiological heterogeneity correlates with clinical prognosis, and our results support this.[3–5,36] In this study, patients with AP-Homo tumors had a lower recurrence rate 2 years postoperatively, presumably because they had a smaller tumor size and a lower frequency of VETC, microvascular invasion, and poor differentiation, which are factors associated with metastatic recurrence.[14] Hyperintensity in the HBP of EOB-MRI was correlated with W/B HCC,[12,19,41] and our results suggest that VETC status in HBP-Hyper and HBP-Iso tumors can be predicted by heterogeneity in HBP (HBP-Hetero vs. HBP-Homo) of EOB-MRI. Our previous report indicated that W/B HCC can be classified into a high-grade group with VETC and a low-grade group without VETC[12]; according to the current results, the former corresponds to HBP-Hetero tumors and the latter to HBP-Homo tumors. Because W/B HCC with VETC expresses high levels of angiopoietin 2 and FGF 2 and is characterized by a paucity of lymphocytic infiltration, HBP-Hetero tumors are expected to be therapeutically responsive to tyrosine kinase inhibitors, such as lenvatinib, but resistant to immunotherapy.[42,43] The report that heterogeneously hyperintense tumors in the hepatobiliary phase of EOB-MRI are resistant to atezolizumab plus bevacizumab therapy[37] can be explained if they are W/B HCC with VETC because such tumors have a paucity of lymphocytes.

Similar to studies featuring radiological detection of VETC using texture analysis,[8–11,44,45] our texture analysis showed that features indicating heterogeneity, such as NonUniformity and Entropy, were higher in VETC$^+$ HCC. Furthermore, visually assessed heterogeneity correlated with VETC and was also validated by texture analysis. The machine learning models for preoperative prediction of VETC proved that enhancement patterns on arterial and hepatobiliary phase images are important features, along with existing reported features such as tumor size, intratumor artery in arterial phase, and non-smooth tumor margin.[11,17] In particular, focusing on tumors with relatively high intensity in the hepatobiliary phase (HBP-Hetero and HBP-Homo), HBP-Hetero tumors had a relatively high rate of VETC positivity, whereas HBP-Homo tumors included few VETC$^+$ HCCs. Because this study was based on surgically resected specimens only, there is a limitation that advanced-stage HCCs were not included. In the future, VETC status and radiological enhancement patterns in advanced-stage HCC should also be investigated.

In conclusion, we have revealed that the classifications of enhancement patterns in the arterial and hepatobiliary phases revealed a correlation between heterogenous enhancement patterns and VETC, whereas spatial histopathological analysis showed that VETC was correlated with local reductions in both AVD and OATP1B3 expression. The pathological evidence we provide here should help to improve the noninvasive prediction of VETC status from radiological images. VETC reflects a unique tumor microenvironment, and knowledge of a tumor's VETC status may contribute to the prediction of prognosis and drug treatment efficacy and thereby aid the formulation of treatment strategies.

AUTHOR CONTRIBUTIONS

Kosuke Matsuda, Akihisa Ueno, and Michiie Sakamoto conceived and designed the study; Kosuke Matsuda, Akihisa Ueno, Yutaka Kurebayashi, Yohei Masugi, Yuta Abe, Yasushi Hasegawa, Minoru Kitago, and Michiie Sakamoto collected the pathological tissue specimens; Kosuke Matsuda, Akihisa Ueno, Junya Tsuzaki, Yutaka

Kurebayashi, Yohei Masugi, Ken Yamazaki, Masashi Tamura, and Michiie Sakamoto collected the data and contributed to data analysis and interpretation; Kosuke Matsuda, Akihisa Ueno, Yutaka Kurebayashi, and Michiie Sakamoto performed the final analysis and drafted the manuscript; Kosuke Matsuda, Akihisa Ueno, Junya Tsuzaki, Yutaka Kurebayashi, Ken Yamazaki, Yohei Masugi, Masashi Tamura, Yuta Abe, Yasushi Hasegawa, Minoru Kitago, Masahiro Jinzaki, and Michiie Sakamoto participated in drafting the article and revising it critically for important intellectual content. Kosuke Matsuda, Junya Tsuzaki, and Akihisa Ueno directly accessed and verified the underlying data reported in the manuscript.

ACKNOWLEDGMENTS

The authors thank all members of Yonken in the Department of Pathology, Keio University School of Medicine, for their support in histological analysis.

FUNDING INFORMATION

This work was supported by JSPS KAKENHI Grant Number JP21K15390 (to Akihisa Ueno) and a research grant from Eisai (to Michiie Sakamoto and Yutaka Kurebayashi). Kosuke Matsuda was supported by the Uehara Memorial Foundation.

CONFLICTS OF INTEREST

Michiie Sakamoto and Yutaka Kurebayashi received research funding from Eisai. The remaining authors have no conflicts to report.

ORCID

Kosuke Matsuda https://orcid.org/0009–0002–7513–038X
Akihisa Ueno https://orcid.org/0000–0001–9428–4128
Junya Tsuzaki https://orcid.org/0009–0007–2398–5593
Yutaka Kurebayashi https://orcid.org/0000–0003–3773–0851
Yohei Masugi https://orcid.org/0000–0002–6952–4043
Ken Yamazaki https://orcid.org/0000–0002–7220–7479
Masashi Tamura https://orcid.org/0000–0002–3762–7144
Yuta Abe https://orcid.org/0000–0002–5840–8901
Yasushi Hasegawa https://orcid.org/0000–0002–4990–0419
Minoru Kitago https://orcid.org/0000–0002–4909–1199
Masahiro Jinzaki https://orcid.org/0000–0002–8241–6565
Michiie Sakamoto https://orcid.org/0009–0005–8242–9824

REFERENCES

1. Llovet JM, Castet F, Heikenwalder M, Maini MK, Mazzaferro V, Pinato DJ, et al. Immunotherapies for hepatocellular carcinoma. Nat Rev Clin Oncol. 2022;19:151–72.
2. Xu X, Zhang HL, Liu QP, Sun SW, Zhang J, Zhu FP, et al. Radiomic analysis of contrast-enhanced CT predicts microvascular invasion and outcome in hepatocellular carcinoma. J Hepatol. 2019;70:1133–44.
3. Brenet Defour L, Mulé S, Tenenhaus A, Piardi T, Sommacale D, Hoeffel C, et al. Hepatocellular carcinoma: CT texture analysis as a predictor of survival after surgical resection. Eur Radiol. 2019;29:1231–9.
4. Kiryu S, Akai H, Nojima M, Hasegawa K, Shinkawa H, Kokudo N, et al. Impact of hepatocellular carcinoma heterogeneity on computed tomography as a prognostic indicator. Sci Rep. 2017;7:12689.
5. Fujita N, Nishie A, Kubo Y, Asayama Y, Ushijima Y, Takayama Y, et al. Hepatocellular carcinoma: Clinical significance of signal heterogeneity in the hepatobiliary phase of gadoxetic acid-enhanced MR imaging. Eur Radiol. 2015;25:211–20.
6. Yang WL, Zhu F, Chen WX. Texture analysis of contrast-enhanced magnetic resonance imaging predicts microvascular invasion in hepatocellular carcinoma. Eur J Radiol. 2022;156:110528.
7. Liu HF, Wang M, Lu YJ, Wang Q, Lu Y, Xing F, et al. CEMRI-based quantification of intratumoral heterogeneity for predicting aggressive characteristics of hepatocellular carcinoma using habitat analysis: Comparison and combination of deep learning. Acad Radiol. 2023;31:2346–55.
8. Yu Y, Fan Y, Wang X, Zhu M, Hu M, Shi C, et al. Radiomics to predict vessels encapsulating tumor clusters (VETC) and patient prognosis in hepatocellular carcinoma. Eur Radiol. 2021;32:959–70.
9. Fan Y, Yu Y, Wang X, Hu M, Du M, Guo L, et al. Texture analysis based on Gd-EOB-DTPA-enhanced MRI for identifying vessels encapsulating tumor clusters (VETC)-positive hepatocellular carcinoma. J Hepatocell Carcinoma. 2021;8:349–59.
10. Fan Y, Yu Y, Hu M, Wang X, Du M, Guo L, et al. Imaging features based on Gd-EOB-DTPA-enhanced MRI for predicting vessels encapsulating tumor clusters (VETC) in patients with hepatocellular carcinoma. Br J Radiol. 2021;94:20200950.
11. Chen FM, Du M, Qi X, Bian L, Wu D, Zhang SL, et al. Nomogram estimating vessels encapsulating tumor clusters in hepatocellular carcinoma from preoperative gadoxetate disodium-enhanced MRI. J Magn Reson Imaging. 2023;57:1893–905.
12. Matsuda K, Kurebayashi Y, Masugi Y, Yamazaki K, Ueno A, Tsujikawa H, et al. Immunovascular microenvironment in relation to prognostic heterogeneity of WNT/β-catenin-activated hepatocellular carcinoma. Hepatol Res. 2023;53:344–56.
13. Kurebayashi Y, Matsuda K, Ueno A, Tsujikawa H, Yamazaki K, Masugi Y, et al. Immunovascular classification of HCC reflects reciprocal interaction between immune and angiogenic tumor microenvironments. Hepatology. 2022;75:1139–53.
14. Fang JH, Zhou HC, Zhang C, Shang LR, Zhang L, Xu J, et al. A novel vascular pattern promotes metastasis of hepatocellular carcinoma in an epithelial-mesenchymal transition-independent manner. Hepatology. 2015;62:452–65.
15. Fang JH, Xu L, Shang LR, Pan CZ, Ding J, Tang YQ, et al. Vessels that encapsulate tumor clusters (VETC) pattern is a predictor of sorafenib benefit in patients with hepatocellular carcinoma. Hepatology. 2019;70:824–39.
16. Lin W, Lu L, Zheng R, Yuan S, Li S, Ling Y, et al. Vessels encapsulating tumor clusters: A novel efficacy predictor of hepatic arterial infusion chemotherapy in unresectable hepatocellular carcinoma. J Cancer Res Clin Oncol. 2023;149:17231–9.
17. Feng Z, Li H, Zhao H, Jiang Y, Liu Q, Chen Q, et al. Preoperative CT for characterization of aggressive macrotrabecular-massive

subtype and vessels that encapsulate tumor clusters pattern in hepatocellular carcinoma. Radiology. 2021;300:219–29.
18. Kim CK, Lim JH, Park CK, Choi D, Lim HK, Lee WJ. Neoangiogenesis and sinusoidal capillarization in hepatocellular carcinoma: Correlation between dynamic CT and density of tumor microvessels. Radiology. 2005;237:529–34.
19. Ueno A, Masugi Y, Yamazaki K, Komuta M, Effendi K, Tanami Y, et al. OATP1B3 expression is strongly associated with Wnt/β-catenin signalling and represents the transporter of gadoxetic acid in hepatocellular carcinoma. J Hepatol. 2014;61:1080–7.
20. Joishi D, Ueno A, Tanimoto A, Okuda S, Masugi Y, Emoto K, et al. Natural course of hypovascular nodules detected on gadoxetic acid-enhanced MR imaging: Presence of fat is a risk factor for hypervascularization. Magn Reson Med Sci. 2013;12:281–7.
21. Rhee H, Cho ES, Nahm JH, Jang M, Chung YE, Baek SE, et al. Gadoxetic acid-enhanced MRI of macrotrabecular-massive hepatocellular carcinoma and its prognostic implications. J Hepatol. 2021;74:109–21.
22. Cerny M, Chernyak V, Olivié D, Billiard JS, Murphy-Lavallée J, Kielar AZ, et al. LI-RADS version 2018 ancillary features at MRI. Radiographics. 2018;38:1973–2001.
23. Tsuboyama T, Onishi H, Kim T, Akita H, Hori M, Tatsumi M, et al. Hepatocellular carcinoma: Hepatocyte-selective enhancement at gadoxetic acid-enhanced MR imaging—Correlation with expression of sinusoidal and canalicular transporters and bile accumulation. Radiology. 2010;255:824–33.
24. WHO Classification of Tumours Editorial Board, 5th Edition, Digestive System Tumours. International Agency for Research on Cancer; 2020.
25. Calderaro J, Couchy G, Imbeaud S, Amaddeo G, Letouze E, Blanc JF, et al. Histological subtypes of hepatocellular carcinoma are related to gene mutations and molecular tumour classification. J Hepatol. 2017;67:727–38.
26. Bedossa P. Intraobserver and interobserver variations in liver biopsy interpretation in patients with chronic hepatitis C. The French METAVIR Cooperative Study Group. Hepatology. 1994;20:15–20.
27. Sato Y, Ojima H, Onaya H, Mori T, Hiraoka N, Kishi Y, et al. Histopathological characteristics of hypervascular cholangiocellular carcinoma as an early stage of cholangiocellular carcinoma. Hepatol Res. 2014;44:1119–29.
28. Hebeler F. Moran's I. MATLAB Central File Exchange. 2024. Accessed October 5, 2024. https://www.mathworks.com/matlabcentral/fileexchange/13663-moran-s-i
29. Dwinnell W. Entropy. MATLAB Central File Exchange. 2024. Accessed October 5, 2024. https://www.mathworks.com/matlabcentral/fileexchange/28692-entropy
30. Rasmussen JH, Olin AB, Lelkaitis G, Hansen AE, Andersen FL, Johannesen HH, et al. Intratumor heterogeneity is biomarker specific and challenges the association with heterogeneity in multimodal functional imaging in head and neck squamous cell carcinoma. Eur J Radiol. 2021;139:109668.
31. Reyes-Aldasoro CC, Williams LJ, Akerman S, Kanthou C, Tozer GM. An automatic algorithm for the segmentation and morphological analysis of microvessels in immunostained histological tumour sections. J Microsc. 2011;242:262–78.
32. Kather JN, Marx A, Reyes-Aldasoro CC, Schad LR, Zöllner FG, Weis CA. Continuous representation of tumor microvessel density and detection of angiogenic hotspots in histological whole-slide images. Oncotarget. 2015;6:19163–76.
33. Tibshirani R. Regression shrinkage and selection via the lasso. J R Stat Soc Ser B: Stat Methodol. 1996;58:267–88.
34. Breiman L. Random forests. Mach Learn. 2001;45:5–32.
35. Ueda K, Matsui O, Kitao A, Kobayashi S, Nakayama J, Miyagawa S, et al. Tumor hemodynamics and hepatocarcinogenesis: Radio-pathological correlations and outcomes of carcinogenic hepatocyte nodules. ISRN Hepatol. 2014;2014:607628.
36. Ariizumi SI, Ban D, Abe Y, Kumamoto T, Koizumi S, Tanabe M, et al. High-signal-intensity MR image in the hepatobiliary phase predicts long-term survival in patients with hepatocellular carcinoma. Anticancer Res. 2019;39:4219–25.
37. Sasaki R, Nagata K, Fukushima M, Haraguchi M, Miuma S, Miyaaki H, et al. Evaluating the role of hepatobiliary phase of gadoxetic acid-enhanced magnetic resonance imaging in predicting treatment impact of lenvatinib and atezolizumab plus bevacizumab on unresectable hepatocellular carcinoma. Cancers (Basel). 2022;14:827.
38. Zhou HC, Liu CX, Pan WD, Shang LR, Zheng JL, Huang BY, et al. Dual and opposing roles of the androgen receptor in VETC-dependent and invasion-dependent metastasis of hepatocellular carcinoma. J Hepatol. 2021;75:900–11.
39. McEwan IJ, Brinkmann AO. Androgen physiology: Receptor and metabolic disorders. In: Feingold KR, Anawalt B, Blackman MR, Boyce A, Chrousos G, Corpas E, eds. Endotext. MDText.com, Inc; 2000.
40. Li CY, Gupta A, Gáborik Z, Kis E, Prasad B. Organic anion transporting polypeptide-mediated hepatic uptake of glucuronide metabolites of androgens. Mol Pharmacol. 2020;98:234–42.
41. Rebouissou S, Franconi A, Calderaro J, Letouzé E, Imbeaud S, Pilati C, et al. Genotype-phenotype correlation of CTNNB1 mutations reveals different ß-catenin activity associated with liver tumor progression. Hepatology. 2016;64:2047–61.
42. Adachi Y, Kamiyama H, Ichikawa K, Fukushima S, Ozawa Y, Yamaguchi S, et al. Inhibition of FGFR reactivates IFNγ signaling in tumor cells to enhance the combined antitumor activity of lenvatinib with anti-PD-1 antibodies. Cancer Res. 2022;82:292–306.
43. Pinyol R, Sia D, Llovet JM. Immune exclusion-Wnt/CTNNB1 class predicts resistance to immunotherapies in HCC. Clin Cancer Res. 2019;25:2021–3.
44. Yang J, Dong X, Wang G, Chen J, Zhang B, Pan W, et al. Preoperative MRI features for characterization of vessels encapsulating tumor clusters and microvascular invasion in hepatocellular carcinoma. Abdom Radiol (NY). 2022;48:554–66.
45. Dong X, Yang J, Zhang B, Li Y, Wang G, Chen J, et al. Deep learning radiomics model of dynamic contrast-enhanced MRI for evaluating vessels encapsulating tumor clusters and prognosis in hepatocellular carcinoma. J Magn Reson Imaging. 2024;59:108–19.

How to cite this article: Matsuda K, Ueno A, Tsuzaki J, Kurebayashi Y, Masugi Y, Yamazaki K, et al. Vessels encapsulating tumor clusters contribute to the intratumor heterogeneity of HCC on Gd-EOB-DTPA-enhanced MRI. Hepatol Commun. 2025;9:e0593. https://doi.org/10.1097/HC9.0000000000000593